

FULLY CONSISTENT DIFFUSION SYNTHETIC ACCELERATION  
OF LINEAR DISCONTINUOUS  $S_N$  TRANSPORT DISCRETIZATIONS  
ON UNSTRUCTURED TETRAHEDRAL MESHES

James. S. Warsa, Todd A. Wareing and Jim E. Morel  
Transport Methods Group  
Los Alamos National Laboratory  
Los Alamos, New Mexico 87545

Send proofs to:

James S. Warsa  
Los Alamos National Laboratory  
CCS-4, MS D409  
Los Alamos, NM 87545

Number of pages: 34  
Number of figures: 7  
Number of tables: 2

E-mail: *warsa@lanl.gov*  
FAX: 505-665-5538

# FULLY CONSISTENT DIFFUSION SYNTHETIC ACCELERATION OF LINEAR DISCONTINUOUS $S_N$ TRANSPORT DISCRETIZATIONS ON UNSTRUCTURED TETRAHEDRAL MESHES

James S. Warsa, Todd A. Wareing and Jim E. Morel

Transport Methods Group

Los Alamos National Laboratory

Los Alamos, New Mexico 87545

## Abstract

We recently presented a method for efficiently solving linear discontinuous discretizations of the two-dimensional  $P_1$  equations on rectangular meshes. The linear system was efficiently solved with Krylov iterative methods and a novel two-level preconditioner based on a linear continuous finite element discretization of the diffusion equation. Here we extend the preconditioned solution method to three-dimensional, unstructured tetrahedral meshes. Solution of the  $P_1$  equations forms the basis of a diffusion synthetic acceleration (DSA) scheme for three-dimensional  $S_N$  transport calculations with isotropic scattering. The  $P_1$  equations and the transport equation are both discretized with isoparametric linear discontinuous finite elements so that the DSA method is fully consistent. Fourier analysis in three dimensions and computational results show that this DSA scheme is stable and very effective. The fully consistent method is compared to other “partially consistent” DSA schemes. Results show that the effectiveness of the partially consistent schemes can degrade for skewed or optically thick mesh cells. In fact, one such scheme can degrade to the extent of being unstable even though it is both unconditionally stable and effective on rectangular grids. Results for a model application show that our fully consistent DSA method can outperform the partially consistent DSA schemes under certain circumstances.

## 1. INTRODUCTION

In this paper, we consider diffusion synthetic acceleration schemes for the linear discontinuous finite element method (DFEM) discretization of the  $S_N$  transport equation on three-dimensional unstructured tetrahedral meshes. See Ref. 1 and references therein for a description of the DFEM for the  $S_N$  equations on unstructured meshes.

For many problems diffusion synthetic acceleration (DSA) is needed to accelerate convergence of the  $S_N$  source iterations.<sup>2,3</sup> It is well known that the discretization of the diffusion equation in a DSA scheme must be “consistent” with the  $S_N$  transport equations discretization in order to be effective and robust for a wide range of problems.<sup>4,5</sup> The effectiveness of a DSA scheme can be measured by the spectral radius of the accelerated algorithm. The spectral radius is always less than one for a useful algorithm. The closer it is to zero the more quickly the iterations converge. Without spatial discretization, the DSA algorithm drastically reduces the spectral radius in highly diffusive problems whose spectral radius would otherwise be close to one.<sup>4,6</sup> In the spatially discretized case, consistency is needed for DSA to achieve this level of effectiveness.

Our fully consistent DSA method is based on a discretization of the  $P_1$  equations using the same linear finite element basis used in the linear DFEM discretization of the  $S_N$  equations on tetrahedral meshes. In both discretizations, discontinuities are introduced by “upwinding” the variables of interest. The linear system of the  $P_1$  discretization is large and sparse. This is because there is a large number (sixteen) of unknowns per cell making direct solution methods impractical even for problems of intermediate size. We therefore solve the discontinuous  $P_1$  equations iteratively with Krylov-subspace methods. Although we only have to store the nonzeros of the sparse matrix the linear system will require significant memory and matrix-vector products can be expensive.

An alternative to consistent DSA schemes are those in which the diffusion equation discretizations are only partially consistent with the transport discretization.<sup>1,7-9</sup> The idea is to reduce the complexity and increase the efficiency of the DSA algorithm. In one case, a scheme with a symmetric positive definite (SPD) linear continuous finite element discretization of the diffusion equation centered on the mesh nodes (vertices) is combined with a prescription to compute (or “update”) the necessary discontinuous quantities on a local, cell-by-cell basis using the continuous diffusion equation solution.<sup>1,7</sup> We will refer to this method as the WLA (Wareing, Larsen and Adams) DSA scheme. The fact that the discretization is centered on the nodes means the linear system can be relatively small because often there are many fewer nodes than cells on unstructured tetrahedral meshes. Because this system is SPD it can be solved by the method of conjugate gradients, which has modest memory requirements and low computational complexity. Thus, the WLA DSA method can be very efficient. In another approach, Larsen’s so-called four step method<sup>4</sup> is modified to find a nonsymmetric linear system for the discontinuous scalar fluxes.<sup>8,9</sup> This is referred to as modified four step (M4S) DSA. Because this method involves only the scalar fluxes, the dimension of the linear system is one

quarter of the dimension of the fully consistent method. Even with the smaller dimension, direct methods can be impractical for large problems. However, a Krylov–subspace iterative method will need less work per iteration than the fully consistent method and the partially consistent diffusion equations can be solved more efficiently.

The increased efficiency of the partially consistent DSA methods can sometimes come at the cost of decreased effectiveness. This can be tolerated as long as the cost of a DSA step is relatively cheap and the degradation in effectiveness is not too extreme. However, partial consistency could result in situations where the DSA method no longer accelerates the transport iterations. We found that the effectiveness of the WLA DSA scheme decreases as the cells in a problem become optically thick and diffusive. We also discovered that in certain problems with skewed cells, the M4S method degrades to the point where it causes the  $S_N$  source iterations to diverge.

Because the DSA scheme we present here is consistent, the spectral radius and, hence, the number of source iterations will be reduced significantly. But it can be competitive with the partially consistent methods only if the solution of the discontinuous  $P_1$  equations can be computed efficiently. We are using a Krylov–subspace iterative solution so we can improve solution efficiency with a good preconditioner. In Ref. 10 we presented a two–level preconditioner for the discontinuous  $P_1$  equations on two–dimensional rectangular meshes. Analysis and numerical experimentation showed that this preconditioner, which is based on a linear continuous finite element discretization of the diffusion equation, was efficient and very effective. We have extended this two–level preconditioned solution technique to the discontinuous  $P_1$  equations on three–dimensional unstructured tetrahedral meshes. The solution method was implemented in the  $S_N$  transport code ATTILAV2<sup>11</sup> as a fully consistent DSA scheme. Our purpose is to discuss the linear DFEM discretization and the two–level preconditioned iterative solution of the  $P_1$  equations. We also investigate the overall efficiency of the accelerated  $S_N$  transport solutions, comparing the fully consistent DSA method to the partially consistent methods.

The remainder of the paper is organized as follows. In the next section we derive a linear DFEM discretization of the  $P_1$  equations on tetrahedral meshes. We then discuss how we solve these equations with a Krylov–subspace iterative method and our two–level preconditioner. The third section presents the details of three–dimensional Fourier analysis on tetrahedra that we use to predict the effectiveness of a DSA scheme. In the fourth section we compare Fourier analysis predictions of the spectral radius to actual measurements of the spectral radius made with ATTILAV2. A moderately sized, realistic example problem is used to measure the computational effort of the accelerated  $S_N$  solution methods. All the results compare the fully consistent DSA method to the partially consistent DSA schemes which have also been implemented in ATTILAV2. The paper concludes with some summary closing remarks.

## 2. DISCONTINUOUS P<sub>1</sub> EQUATIONS ON TETRAHEDRAL MESHES

In this section, we will derive a DFEM discretization for the diffusion equation by noting that the (time-independent) system of coupled, first order P<sub>1</sub> equations and the second order diffusion equation are equivalent. We can then discretize the first order system with a linear DFEM similar to that used for the S<sub>N</sub> transport equation. The difference is that the angular flux unknown associated with the transport operator is naturally identified with a unique direction of particle flow. These flow directions facilitate the introduction of discontinuities into the discretization. In contrast, quantities corresponding to particle flows do not exist naturally in the P<sub>1</sub> system. Instead, the particle flows are *defined* using one of several possible approaches.<sup>8–10, 12</sup>

There has recently been a great deal of interest and activity in the applied mathematics community relating to the development of discontinuous Galerkin methods for the discretization of partial differential equations.<sup>13</sup> To connect with this literature, we point out that the linear DFEM discretization of the S<sub>N</sub> transport equation can be viewed as a linear discontinuous, Galerkin finite element method, denoted by dG(1). Similarly, our consistent DFEM discretization of the P<sub>1</sub> equations can be viewed as a “mixed” dG(1) method for the diffusion equation.<sup>12</sup> The numerical analysis of mixed discontinuous methods for elliptic operators, like the diffusion operator, is an active area of research.

This section begins by describing the discontinuous DFEM discretization of the P<sub>1</sub> equations on tetrahedra. This is followed by a description of the two-level preconditioning technique using a linear continuous discretization of the diffusion equation. A brief discussion of the DSA algorithm follows that, and the section concludes with ways to improve the efficiency of the DSA algorithm.

### 2.1 The Discretized Equations

The steady-state P<sub>1</sub> equations in three-dimensional geometry are

$$\frac{1}{3} \nabla \Phi(\mathbf{r}) + \sigma_t(\mathbf{r}) \mathbf{J}(\mathbf{r}) = \mathbf{Q}_1(\mathbf{r}), \quad (1a)$$

$$\nabla \cdot \mathbf{J}(\mathbf{r}) + \sigma_a(\mathbf{r}) \Phi(\mathbf{r}) = Q_0(\mathbf{r}). \quad (1b)$$

The usual particle transport notation is used here:  $\Phi(\mathbf{r})$  represents the scalar flux (zeroth angular moment of the angular flux),  $\mathbf{J}(\mathbf{r})$  represents the current vector (first angular moment of the angular flux), and  $\mathbf{r} \in V$  is the position vector in some domain  $V$ . The source terms  $Q_0(\mathbf{r})$  and  $\mathbf{Q}_1(\mathbf{r})$  are the zeroth and first angular moments of an inhomogeneous source, a material property. It is often assumed the material emits particles isotropically such that  $\mathbf{Q}_1(\mathbf{r})$  is zero. The first expression is a vector equation referred to as the first moment equation(s). The second is called the balance equation. For clarity they will consistently be written in this order.

Boundary conditions for the  $P_1$  equations are specified by separating the flow of particles through a surface into inwardly and outwardly directed flows. One way to do this is to use the  $P_1$  approximation itself and assume the angular flux is linear in angle:  $\Psi(\mathbf{r}, \hat{\Omega}) = \frac{1}{4\pi}\Phi(\mathbf{r}) + \frac{3}{4\pi}\hat{\Omega} \cdot \mathbf{J}(\mathbf{r})$ . Under this approximation, the inwardly directed flow (partial current) of particles through a surface located at  $\mathbf{r}_s$  with outward unit normal  $\hat{n}$  can be expressed as

$$J^{in}(\mathbf{r}_s) = \int_{(\hat{n} \cdot \hat{\Omega}) < 0} (\hat{n} \cdot \hat{\Omega}) \Psi(\mathbf{r}_s, \hat{\Omega}) d\Omega = \frac{1}{4}\Phi(\mathbf{r}_s) - \frac{1}{2}\hat{n} \cdot \mathbf{J}(\mathbf{r}_s), \quad (2a)$$

and an outwardly directed flow as

$$J^{out}(\mathbf{r}_s) = \int_{(\hat{n} \cdot \hat{\Omega}) > 0} (\hat{n} \cdot \hat{\Omega}) \Psi(\mathbf{r}_s, \hat{\Omega}) d\Omega = \frac{1}{4}\Phi(\mathbf{r}_s) + \frac{1}{2}\hat{n} \cdot \mathbf{J}(\mathbf{r}_s). \quad (2b)$$

We will consider vacuum or reflection boundary conditions. For vacuum conditions, assume no external angular flux of particles enters the through the external boundary surface,  $\partial V \subset V$ , that is,  $\Psi(\mathbf{r}_s, \hat{\Omega}) = 0$  for  $\mathbf{r}_s \in \partial V$  and  $(\hat{n} \cdot \hat{\Omega}) < 0$ . Then the vacuum condition, or Marshak boundary condition, relates the scalar flux and currents on the boundary through Eq. 2a by setting  $J^{in}(\mathbf{r}_s) = 0$  for  $\mathbf{r}_s \in \partial V$ . Reflection boundary conditions are specified by simply setting  $J^{in}(\mathbf{r}_s) = J^{out}(\mathbf{r}_s)$ . We will also need Eqs. 2 later when we “upwind” our discontinuous discretization.

We can construct the DFEM discretization of the  $P_1$  equations by defining a linear finite element basis on a tetrahedral cell  $T_k \in V$ . A local ordering of the faces and vertices of a cell is established such that face  $i$  is the face opposite from vertex  $i$ . The bases  $L_i, i = 1, 4$  are defined in terms of local coordinates  $(u, v, w)$  and can be mapped to and from the global coordinate system as follows. On the “master” tetrahedron, illustrated in Fig. 1, the barycentric coordinates are

$$L_1 = u, \quad (3a)$$

$$L_2 = v, \quad (3b)$$

$$L_3 = w, \quad (3c)$$

$$L_4 = 1 - L_1 - L_2 - L_3 = 1 - u - v - w, \quad (3d)$$

Their use simplifies the derivation and is easily generalized to higher order elements. The linear basis function we use here are just the barycentric coordinates themselves. Each of them are unity at their respective vertices and zero at the other three vertices. Together with Eqs. 3, the mapping between the global Cartesian coordinates of the mesh vertices, as illustrated in Fig. 2 for example, and the local barycentric coordinates can be established by representing the global coordinates  $\mathbf{r} = (x, y, z)$  in terms of a linear combination the

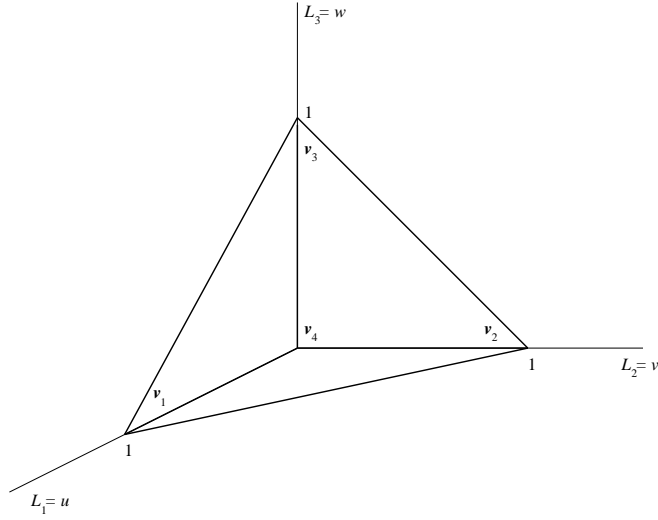


Figure 1. The master tetrahedron with vertices in  $(u,v,w)$  coordinates at  $\mathbf{v}_1 = (1,0,0)$ ,  $\mathbf{v}_2 = (0,1,0)$ ,  $\mathbf{v}_3 = (0,0,1)$ , and  $\mathbf{v}_4 = (0,0,0)$ . The local coordinate axes are the barycentric coordinates  $L_1$ ,  $L_2$  and  $L_3$  (the fourth barycentric coordinate is not shown).

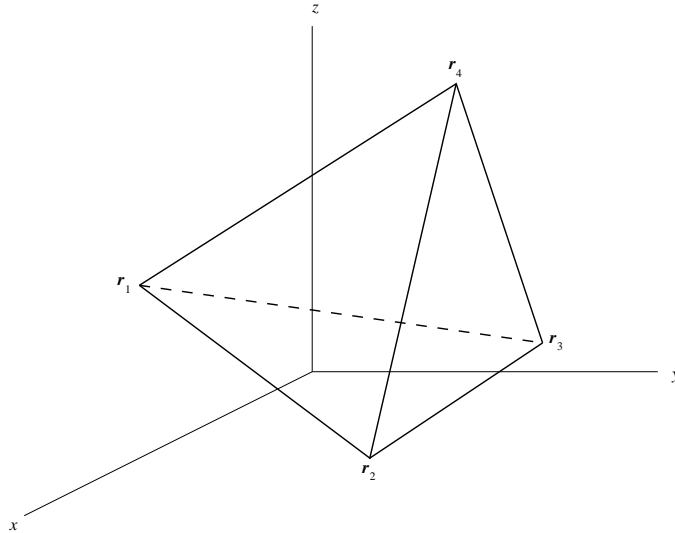


Figure 2. A tetrahedron in the global coordinate space  $\mathbf{r} = (x, y, z)$  with four vertices  $\mathbf{r}_1, \mathbf{r}_2, \mathbf{r}_3, \mathbf{r}_4$ .

barycentric coordinates  $(L_1, L_2, L_3, L_4)$  as follows:

$$x = L_1 x_1 + L_2 x_2 + L_3 x_3 + L_4 x_4 \quad (4a)$$

$$y = L_1 y_1 + L_2 y_2 + L_3 y_3 + L_4 y_4 \quad (4b)$$

$$z = L_1 z_1 + L_2 z_2 + L_3 z_3 + L_4 z_4 \quad (4c)$$

$$1 = L_1 + L_2 + L_3 + L_4. \quad (4d)$$

More on the use of barycentric coordinates can be found in Ref. 14.

Now we expand the scalar fluxes and currents on a cell in terms of the basis functions. These approximations are respectively denoted by  $\Phi_h$  and  $\mathbf{J}_h$ . The general discrete problem reads as follows:

compute the approximations  $\Phi_h$  and  $\mathbf{J}_h$  on a cell  $T_k$  satisfying

$$\frac{1}{3} \int_{\partial T_k} \Phi_h^b (\hat{n} \cdot \mathbf{w}_h) dS - \frac{1}{3} \int_{T_k} \Phi_h (\nabla \cdot \mathbf{w}_h) dV + \sigma_{t,k} \int_{T_k} \mathbf{J}_h \cdot \mathbf{w}_h dV = \int_{T_k} \mathbf{Q}_1 \cdot \mathbf{w}_h dV, \quad (5a)$$

$$\int_{\partial T_k} (\hat{n} \cdot \mathbf{J}_h^b) u_h dS - \int_{T_k} \mathbf{J}_h \cdot \nabla u_h dV + \sigma_{a,k} \int_{T_k} \Phi_h u_h dV = \int_{T_k} Q_0 u_h dV, \quad (5b)$$

for all trial functions  $u_h$  and  $\mathbf{w}_h$ .

We have used the divergence theorem to integrate terms involving gradients. This is necessary for introducing the discontinuous approximation.

The linear trial space consists of the four scalar trial functions  $u_h$ , which are just the four basis function  $L_i$  written in terms of the global coordinate system. The four vector trial functions  $\mathbf{w}_h$ , are also written in terms of these basis functions as  $L_i \hat{i} + L_i \hat{j} + L_i \hat{k}$  for  $i = 1, \dots, 4$ , where  $\hat{i}, \hat{j}$  and  $\hat{k}$  are unit basis vectors that point in the direction of the positive  $x$ ,  $y$  and  $z$  axes, respectively. Equations 5 are written at the vertex of every cell. The vector equation, Eq. 5a, is written separately for each of the  $x$ ,  $y$ , and  $z$  components at the four cell vertices. The result is sixteen equations in sixteen unknowns for every cell in the mesh. The unknowns are the values of flux,  $\Phi_{i,k}$  and three current components  $J_i^x$ ,  $J_i^y$ , and  $J_i^z$  at the four cell vertices,  $i = 1, 4$ . The flux and currents are discontinuous, defined separately in each cell as the limiting values of  $\Phi(\mathbf{r})$  and  $\mathbf{J}(\mathbf{r})$  as  $\mathbf{r} \rightarrow \mathbf{r}_i$  from within the cell.

The integrals over the boundary of the tetrahedral cells,  $\partial T_k$ , contain the quantities  $\Phi_h^b$  and  $(\hat{n} \cdot \mathbf{J}_h^b)$ , indicating that they are “boundary” terms. They are uniquely defined in terms of the particle flows through the cell faces, using a linear combination of the discrete discontinuous unknowns from the two adjacent cells sharing a particular face. The three discontinuous values of the scalar flux and currents on the cell face of a particular cell are used to define the outgoing particle flow through the face. The three discontinuous values of the flux and currents from the adjacent cell that shares the face are used to define the incoming particle flow through the face. If the face of a cell constitutes an external boundary, the incoming flow is specified according to the boundary conditions.

The integrations of the boundary terms in Eqs. 5 give rise to expressions of the form  $\hat{n}_j \Phi_i^b$  and  $(\hat{n}_j \cdot \mathbf{J}_i^b)$  at three vertices  $i$  on a face  $j$  with outward normal  $\hat{n}_j$ . One way to define the upwind particle flows for the discontinuous discretization is to use discrete versions of the partial currents as follows. Adding and



subtracting the continuous partial currents we can write

$$\Phi_h^b = 2 (J^{out} + J^{in}) \quad (6a)$$

$$(\hat{n} \cdot J_h^b) = J^{out} - J^{in}. \quad (6b)$$

Use these relationships for vertex  $i$  and specify boundary conditions by setting  $\xi_j$  according to

$$\xi_j = \begin{cases} 0 & \text{if face } j \text{ is vacuum or internal,} \\ 1 & \text{if face } j \text{ is reflective,} \end{cases}$$

to get the necessary quantities:

$$\hat{n}_j \Phi_i^b = 2 \hat{n}_j \left( J_{j,i}^{out} [1 + \xi_j] + J_{j,i}^{in} [1 - \xi_j] \right) \quad (7a)$$

$$(\hat{n}_j \cdot J_i^b) = \left( J_{j,i}^{out} - J_{j,i}^{in} \right) [1 - \xi_j]. \quad (7b)$$

The particle flow definitions are completed by defining the partial currents in these last expressions. The flows into and out of face  $j$  at vertex  $i$  are

$$J_{j,i}^{in} = \frac{1}{4} \Phi_i^{ext} - \frac{1}{2} \hat{n}_j \cdot \mathbf{J}_i^{ext} \quad (7c)$$

$$J_{j,i}^{out} = \frac{1}{4} \Phi_i + \frac{1}{2} \hat{n}_j \cdot \mathbf{J}_i, \quad (7d)$$

where “*ext*” denotes exterior quantities. They are the quantities from the adjacent cell that shares face  $j$  with cell  $k$  and “across” the face from vertex  $i$ .

Another way to define the upwinded boundary terms is borrowed from computational fluid dynamics.<sup>15, 16</sup> Consider the homogeneous, time-dependent P<sub>1</sub> equations in a void,

$$\frac{\partial \Phi(\mathbf{r}, t)}{\partial t} + \nabla \cdot \mathbf{J}(\mathbf{r}, t) = 0, \quad (8a)$$

$$\frac{\partial \mathbf{J}(\mathbf{r}, t)}{\partial t} + \frac{1}{3} \nabla \Phi(\mathbf{r}, t) = 0, \quad (8b)$$

and the advection of a plane wave with wave number  $\kappa$  oriented in the normalized direction  $\hat{n} = n_x \hat{i} + n_y \hat{j} + n_z \hat{k}$ ,

$$u(\mathbf{r}, t) = \begin{bmatrix} \Phi(\mathbf{r}, t) \\ J^x(\mathbf{r}, t) \\ J^y(\mathbf{r}, t) \\ J^z(\mathbf{r}, t) \end{bmatrix} = \begin{bmatrix} \alpha_0(t) \\ \alpha_x(t) \\ \alpha_y(t) \\ \alpha_z(t) \end{bmatrix} e^{i\kappa(\hat{n} \cdot \mathbf{r})} \equiv \alpha(t) e^{i\kappa(\hat{n} \cdot \mathbf{r})}. \quad (9)$$

Equations 8 can then be written as a first-order vector wave equation

$$\alpha_t + i\kappa \mathbf{H} \alpha(t) = 0, \quad (10)$$

the subscript  $t$  denoting a time derivative. The matrix

$$\mathbf{H} = \begin{bmatrix} 0 & n_x & n_y & n_z \\ \frac{1}{3}n_x & 0 & 0 & 0 \\ \frac{1}{3}n_y & 0 & 0 & 0 \\ \frac{1}{3}n_z & 0 & 0 & 0 \end{bmatrix} \quad (11)$$

is then diagonalized such that  $\mathbf{H} = \mathbf{R} \mathbf{\Lambda} \mathbf{R}^{-1}$ , where

$$\mathbf{R} = \begin{bmatrix} 1 & 1 & 0 & 0 \\ \frac{1}{\sqrt{3}}n_x & -\frac{1}{\sqrt{3}}n_x & 1 & 0 \\ \frac{1}{\sqrt{3}}n_y & -\frac{1}{\sqrt{3}}n_y & 0 & 1 \\ \frac{1}{\sqrt{3}}n_z & -\frac{1}{\sqrt{3}}n_z & -\frac{n_x}{n_z} & -\frac{n_y}{n_z} \end{bmatrix} \quad (12a)$$

$$\mathbf{R}^{-1} = \begin{bmatrix} \frac{1}{2} & \frac{\sqrt{3}}{2}n_x & \frac{\sqrt{3}}{2}n_y & \frac{\sqrt{3}}{2}n_z \\ \frac{1}{2} & -\frac{\sqrt{3}}{2}n_x & -\frac{\sqrt{3}}{2}n_y & -\frac{\sqrt{3}}{2}n_z \\ 0 & (n_y^2 + n_z^2) & -n_x n_y & -n_x n_z \\ 0 & -n_x n_y & (n_x^2 + n_z^2) & -n_y n_z \end{bmatrix} \quad (12b)$$

and  $\mathbf{\Lambda} = \text{diag}(\frac{1}{\sqrt{3}}, -\frac{1}{\sqrt{3}}, 0, 0)$  is the diagonal matrix of eigenvalues of  $\mathbf{H}$ .

Multiplying Eq. 10 through by  $\mathbf{R}^{-1}$  we get

$$\beta_t + i\kappa \mathbf{\Lambda} \beta(t) = 0, \quad (13)$$

where  $\beta(t) = \mathbf{R}^{-1} \alpha(t)$ . Because  $\mathbf{\Lambda}$  is diagonal the solutions of Eq. 13 decouple, leading to

$$\beta(t) = \beta(0) e^{-i\kappa \lambda_j t}, \quad j = 1, 4. \quad (14)$$

Noting that  $\alpha(t) = \mathbf{R} \beta(t)$ , we can multiply this through by  $\mathbf{R}$  to find the solutions

$$\alpha(t) = \alpha(0) e^{-i\kappa \lambda_j t}, \quad j = 1, 4, \quad (15)$$

for some initial amplitude  $\alpha(0)$ .

Therefore, under the transformation to “characteristic variables”,  $v(t) = \mathbf{R}^{-1} u(t)$ , plane waves are prop-

agated with (constant) wave-speeds defined by the non-zero eigenvalues  $\pm \frac{1}{\sqrt{3}}$ . Now, this is useful to us even in the time-independent case because we can identify “flow directions” with these eigenvalues relative to the direction vector of the plane wave,  $\hat{n}$ . If this direction is taken to be the outward normal vector of some surface, we associate outwardly directed flows through that surface with the positive eigenvalue and inwardly directed flows with the negative eigenvalue. Transformation of the (time-independent) solution vector  $\left[ \Phi(\mathbf{r}), J^x(\mathbf{r}), J^y(\mathbf{r}), J^z(\mathbf{r}) \right]^T$  to characteristic variables gives the expressions

$$J^\pm = \frac{1}{2} \Phi(\mathbf{r}) \pm \frac{\sqrt{3}}{2} \hat{n} \cdot \mathbf{J}(\mathbf{r}) \quad (16)$$

that correspond to outwardly and inwardly directed flows, respectively. These equations can be used to define the “boundary” terms in Eqs. 5, as an alternative to Eqs. 2. Adding and subtracting these expressions gives

$$\Phi_h^b = (J^+ + J^-) \quad (17a)$$

$$(\hat{n} \cdot \mathbf{J}_h^b) = \frac{1}{\sqrt{3}} (J^+ - J^-). \quad (17b)$$

For a given face  $j$  and vertex  $i$  on some cell  $k$ , we find

$$\hat{n}_j \Phi_i^b = \hat{n}_j \left( J_{j,i}^{out} [1 + \xi_j] + J_{j,i}^{in} [1 - \xi_j] \right) \quad (18a)$$

$$(\hat{n}_j \cdot \mathbf{J}_i^b) = \frac{1}{\sqrt{3}} \left( J_{j,i}^{out} - J_{j,i}^{in} \right) [1 - \xi_j], \quad (18b)$$

where the flows into and out of the face are given by

$$J_{j,i}^{in} = \frac{1}{2} \Phi_i^{ext} - \frac{\sqrt{3}}{2} \hat{n}_j \cdot \mathbf{J}_i^{ext} \quad (18c)$$

$$J_{j,i}^{out} = \frac{1}{2} \Phi_i + \frac{\sqrt{3}}{2} \hat{n}_j \cdot \mathbf{J}_i. \quad (18d)$$

No matter what choice is made for defining the particle flows, we order the unknowns on the mesh first by the current vector for each vertex on every cell, followed by the scalar flux for each vertex on every cell. Then we can write the linear system in the  $(2 \times 2)$  block form

$$\begin{bmatrix} \mathbf{A}_t & \frac{1}{3} \mathbf{A}_0 \\ -\mathbf{A}_0^T & \mathbf{A}_a \end{bmatrix} \begin{bmatrix} \mathbf{J} \\ \Phi \end{bmatrix} = \begin{bmatrix} \mathbf{f} \\ g \end{bmatrix}, \quad (19)$$

We have observed that the submatrices  $\mathbf{A}_t$  and  $\mathbf{A}_a$  are symmetric positive definite (SPD). Hence the system

can also be written in the symmetric indefinite form

$$\begin{bmatrix} 3\mathbf{A}_t & \mathbf{A}_0 \\ \mathbf{A}_0^T & -\mathbf{A}_a \end{bmatrix} \begin{bmatrix} \mathbf{J} \\ \Phi \end{bmatrix} = \begin{bmatrix} 3\mathbf{f} \\ -g \end{bmatrix}, \quad (20)$$

Finally, we note that we can compute a Schur complement,  $\mathbf{S}$ , of the  $(2 \times 2)$  block linear systems above. It is formed by block Gaussian elimination (which can be viewed as eliminating the currents in favor of the scalar fluxes) resulting in the SPD linear system

$$\mathbf{S}\Phi = [\mathbf{A}_a + \mathbf{A}_0^T(3\mathbf{A}_t)^{-1}\mathbf{A}_0]\Phi = g + 3[(3\mathbf{A}_t)^{-1}\mathbf{A}_0]\mathbf{f}, \quad (21)$$

for the discontinuous scalar fluxes only. On tetrahedra this reduced system involves 1/4 the number of unknowns of the original full  $P_1$  system of equations. This is potentially a tremendous savings for transport acceleration since only the scalar fluxes are needed for that purpose and the method of conjugate gradients (CG) can be used to solve the reduced linear system. We would not form the reduced system directly because the discontinuous approximation introduced into the discretization leads to a globally coupled system. That is, the inverse  $(3\mathbf{A}_t)^{-1}$  is dense and, therefore, so is the Schur complement. Instead we can implicitly compute the “action” of the Schur complement as needed. Iterative solution algorithms supply vectors  $u$  for which the matrix–vector product  $v = \mathbf{S}u$  is to be returned to the algorithm. We compute the action of the Schur complement by first calculating  $s = \mathbf{A}_0 u$  for a given vector  $u$ . Then we use an inner iteration to approximately calculate  $t = (3\mathbf{A}_t)^{-1}s$  and complete the computation by calculating  $v = \mathbf{A}_a u + \mathbf{A}_0^T t$ . Even though the CG algorithm is used for both SPD linear systems we have found that a combined inner–outer iteration is not as efficient as our methods for solving the full system. One way to remedy this could be to compute the Cholesky factorization of the  $\mathbf{A}_t$  block which is first reordered for minimum fill-in. Then, instead of an inner iteration, the action the Schur complement simply requires a forward and backward substitution at every outer CG iteration. The cost of computing the factorization is amortized over the course of the CG iterations and the Schur complement matrix–vector computation will be very fast once we have stored the factorization. A drawback is that the Cholesky factorization is not necessarily efficient on parallel platforms. Furthermore, the fill-in associated with the factorization increases memory requirements. We plan to explore solution of the reduced system in the future.

## 2.2 Solution Methods

The discontinuous  $P_1$  equations, Eq. 19 or Eq. 20, form an sparse linear system,  $\mathbf{A}x = b$ . To be used as part of a DSA scheme, we must solve this system efficiently. For large problems direct methods are infeasible, so we use iterative solution techniques to which we can apply multilevel acceleration methods. Iterative

solution methods also allow us to take advantage of the sparsity of the linear system by storing only the nonzeros of the matrix.

Our solution technique consists of a two-level iteration. An outer Krylov-subspace iterative method is used to solve the discontinuous  $P_1$  equations. To compute the iterative solution efficiently, a preconditioner  $\mathbf{M}$  is needed that can adequately alter the spectrum of the original matrix  $\mathbf{A}$ . Loosely speaking, the preconditioner will be effective if the eigenvalues of the preconditioned matrix  $\mathbf{M}^{-1}\mathbf{A}$  are clustered and bounded away from the origin.<sup>17</sup> We have found that the convergence rate of the outer Krylov iteration improves if the condition number, measured by the ratio of the maximum to minimum singular values of  $\mathbf{M}^{-1}\mathbf{A}$ , is smaller than that of the original system. This is only a rough indicator of preconditioner effectiveness.<sup>10,18</sup> A preconditioner for the discontinuous  $P_1$  equations on two-dimensional rectangular meshes was presented in Ref. 10. We have extended the method to three-dimensional unstructured tetrahedral meshes. The preconditioner uses a linear continuous finite element discretization of the diffusion equation. Solution of the corresponding linear system is the second level of our two-level preconditioning technique.

In Ref. 10 we showed that the two-level preconditioner on rectangular meshes was effective over a wide range of problems and seems to be particularly well-suited to solving problems which are optically thick and diffusive. This is fortunate because these happen to be just the kinds of problems for which we would like to solve the  $P_1$  equations as part of a transport acceleration algorithm. Using the linear continuous discretization for the diffusion equation as a preconditioner was suggested by the observation that discontinuities in the  $P_1$  solution disappear as the problem becomes optically thick and diffusive. The preconditioner scaled very well with problem size in two dimensional geometry with rectangular meshes but the convergence rates of both the inner and outer iterations degraded for cells that are very optically thin in one or both dimensions.

At every iteration, the Krylov solver supplies a vector  $r$  requesting that a vector  $z = \mathbf{M}^{-1}r$  be returned to the solver. In our case, this is computed implicitly. That is, we “solve”  $\mathbf{M}z = r$  for  $z$  without explicitly forming or inverting a matrix  $\mathbf{M}$ . This will be made clearer if one examines our two-level approach as displayed in Algorithm 1.

---

**Algorithm 1.** Two-Level Preconditioner

---

```

 $z \leftarrow 0$ 
 $s \leftarrow r - \mathbf{A}z$ 
 $z \leftarrow z + \omega \tilde{\mathbf{A}}^{-1}s$ 
 $s \leftarrow r - \mathbf{A}z$ 
 $z \leftarrow z + \mathbf{C}^{-1}s$ 
 $s \leftarrow r - \mathbf{A}z$ 
 $z \leftarrow z + \omega \tilde{\mathbf{A}}^{-1}s$ 

```

---

The algorithm consists of three distinct steps, giving it the character of a two-stage multigrid V-cycle. Solution of the linear continuous finite element discretization of the diffusion equation, denoted by the operator  $\mathbf{C}^{-1}$ , resides at the lowest level. It is preceded and followed smoothing iterations, where  $\tilde{\mathbf{A}}$  is some simple approximation to  $\mathbf{A}$ . It is this entire series of computations that is implicitly represented by the operator  $\mathbf{M}^{-1}$  acting on some vector  $r$ .

The operator  $\mathbf{C}^{-1}$  in Algorithm 1 is computed implicitly as well. The diffusion equation is discretized using linear continuous finite elements such that unknowns are located on the mesh vertices. The linear system corresponding to this discretization is of lower dimension ( $\mathbb{R}^{N_v}$ , with  $N_v$  being the number of vertices in the mesh) than that of the discontinuous  $P_1$  equations ( $\mathbb{R}^{16N_c}$ , where  $N_c$  is the number of cells in the mesh). Note that typical tetrahedral meshes contain roughly four or five times as many cells as vertices. The computation of  $\mathbf{C}^{-1}$  therefore consists of three steps: a projection, a matrix inversion, and an interpolation, written symbolically as  $\mathbf{C}^{-1} = \mathbf{Q}\mathbf{D}^{-1}\mathbf{P}$ . The matrix  $\mathbf{P}$  projects from  $\mathbb{R}^{16N_c}$  onto  $\mathbb{R}^{N_v}$  and the matrix  $\mathbf{Q}$  interpolates back again. The projections are computed as a source term for each cell-vertex centered diffusion equation by summing an appropriate combination of the discontinuous scalar flux and current residuals from all the cells surrounding a vertex. This is discussed in more detail below. The interpolations simply assign the same continuous diffusion equation solution to all the discontinuous scalar fluxes surrounding a particular vertex; the currents are left unchanged. The matrix  $\mathbf{D}^{-1}$  represents the inverse of the linear continuous diffusion equations which is computed approximately using preconditioned conjugate gradients (PCG) with simple diagonal preconditioning.

The smoothing operator (matrix)  $\tilde{\mathbf{A}}$  is either the block-diagonal matrix extracted from the discontinuous  $P_1$  matrix on a cell-by-cell basis, represented by  $\mathbf{B}$ , or it is the identity  $\mathbf{I}$ . For the former case, the smoother is a block-Jacobi iteration and in the latter case it is a Richardson iteration. In the block-Jacobi iteration, each block is a  $(16 \times 16)$  matrix representing the coupling between all the unknowns (scalar fluxes and currents) on a cell. Each block can be evaluated independently, one cell at a time, which could potentially be very efficient in a parallel implementation. Overall, the preconditioner with Richardson smoothing is less efficient than with block-Jacobi smoothing. In this paper we consider only  $\tilde{\mathbf{A}} = \mathbf{B}$ .

Manipulation of the  $P_1$  equations leads to a source term that represents the “correct” projection operator. We start by assuming the discontinuous unknowns in the  $P_1$  equations are continuous at the vertices. We then write the balance equations and moment equations (in vector form) for the four vertices on some cell  $k$ . The right hand side of the  $P_1$  equations is set to a “residual” vector of the discontinuous operator; referring to Algorithm 1 this vector is  $s = r - \mathbf{A}z$ , where  $z$  is the updated vector from the first block Jacobi iteration. The four moment equations are added together to find an expression for the average current vector on a cell, noting that the area vectors of a cell sum to zero and that the outwardly directed area vectors for a face shared by two cells are the negative of one another. The expression for the average current appears in the

four balance equations on a cell. Inserting that expression into the balance equation for vertex  $j$  on cell  $k$  gives

$$\frac{\mathbf{a}_j}{27\sigma_{t,k}V_k} \cdot \left( \sum_{i=1}^4 \mathbf{a}_i \phi_i \right) + \frac{\sigma_{a,k}V_k}{20} \left( 2\phi_j + \sum_{\substack{i=1 \\ i \neq j}}^4 \phi_i \right) = s_{j,k} - \frac{\mathbf{a}_j}{3\sigma_{t,k}V_k} \cdot \left( \sum_{i=1}^4 \mathbf{s}_{i,k} \right), \quad (22)$$

which is the linear continuous finite element discretization of the diffusion equation. The right hand side is the projection of the discontinuous residual vector  $s$ , where  $s_{j,k}$  is the residual in the scalar flux at vertex  $j$  in cell  $k$ , the terms  $\mathbf{s}_{i,k}$  are the residuals in the currents at all vertices  $i$  in cell  $k$ , and  $\mathbf{a}_j = \hat{n}_j a_j$  is the “area vector” of a face  $j$  having outward normal  $\hat{n}_j$  and area  $a_j$ . The continuous unknowns,  $\phi_n$ , are given the global ordering of the mesh vertices. Every mesh vertex is shared by an arbitrary number of cells and Eq. 22 is computed for the corresponding local vertex  $j$  on each of those cells. The equations are summed over the surrounding cells, each one contributing to the coefficients of the continuous diffusion matrix,  $\mathbf{D}$ , for the row corresponding to that global vertex. The projection operation in an implementation follows from this summation.

We use GMRES( $m$ ) for computing the solution of the discontinuous  $P_1$  equations if either the linear system or the preconditioner is not symmetric.<sup>19</sup> The projection operator and simple interpolation method we use makes the preconditioner nonsymmetric, that is,  $\mathbf{Q} \neq \mathbf{P}^T$ . We could also to use a solution method appropriate for symmetric indefinite linear systems, such as MINRES or SYMMLQ, to solve the symmetric indefinite form of the  $P_1$  equations.<sup>20</sup> These linear solvers require the preconditioner to be SPD and we can impose symmetry by *defining*  $\mathbf{Q} = \mathbf{P}^T$ . We can ensure that the preconditioner is positive definite by scaling the problem by some norm of the linear system. However, while these solvers are more efficient than GMRES in terms of both the work required per iteration and storage requirements, imposing symmetry turned out to degrade the effectiveness of the two-level preconditioner offsetting any potential savings in computational effort. In the results reported here, we use GMRES( $m$ ) to solve the discontinuous  $P_1$  equations in nonsymmetric form with the nonsymmetric preconditioner.

### 2.3 Diffusion Synthetic Acceleration

We now present a brief description of the diffusion synthetic accelerated iterative transport solution method.

The DFEM discretization of the  $S_N$  transport equation uses the same linear basis functions as the  $P_1$  equations. We assume an angular quadrature  $\{\hat{\Omega}_m, w_m\}$  whose weights sum to unity and consider isotropic scattering only. An inhomogeneous (isotropic) distributed source,  $Q_m$  may also be specified. The angular flux on a cell  $k$  expanded in terms of the basis functions is denoted by  $\psi_{m,h}$  and the discrete problem reads as follows.

For each angle  $\hat{\Omega}_m$  find an approximation to the angular flux on a cell  $k$ ,  $\psi_{m,h}$  satisfying

$$\begin{aligned} \hat{\Omega}_m \cdot \left( \int_{\partial T_k} \hat{n} \psi_m^b u_h \, dS - \int_{T_k} \psi_{m,h}^{\ell+1} \nabla u_h \right) dV + \sigma_{tk} \int_{T_k} \psi_{m,h}^{\ell+1} u_h \, dV \\ = \sigma_{sk} \sum_m w_m \int_{T_k} \psi_{m,h}^\ell u_h \, dV + \int_{T_k} Q_m u_h \, dV \end{aligned} \quad (23)$$

for all trial functions  $u_h$ .

The trial functions are again just the four linear tetrahedral basis functions  $L_i$ . These expressions are computed for each vertex  $j$  on a cell  $k$ , giving four equations in four unknowns on every cell. The integrations over the boundary of the tetrahedron  $\partial T_k$  give rise to terms having the form  $(\hat{\Omega}_m \cdot \mathbf{n}_j) \psi_{m,j}^b$ . These are replaced by upwinding or with the boundary conditions, specified by some function  $\Gamma(\hat{\Omega})$ , as follows. For a cell  $k$  and face  $j$  we set

$$(\hat{\Omega}_m \cdot \hat{n}_j) \psi_{m,j}^b = \begin{cases} (\hat{\Omega}_m \cdot \hat{n}_j) \psi_{m,j,k}^{\ell+1}, & \hat{\Omega}_m \cdot \hat{n}_j > 0, \quad \forall \text{ faces } j \text{ in } V \\ (\hat{\Omega}_m \cdot \hat{n}_j) \psi_{m,i,j}^{ext}, & \hat{\Omega}_m \cdot \hat{n}_j < 0, \quad \text{face } j \text{ in } V \setminus \partial V \\ \Gamma(\hat{\Omega}_m), & \hat{\Omega}_m \cdot \hat{n}_j < 0, \quad \text{face } j \text{ in } \partial V, \end{cases} \quad (24)$$

where the “external” flux  $\psi_{i,j}^{ext}$  is the value of the angular flux across the face  $j$  from vertex  $i$  in the neighboring cell that shares face  $j$  with cell  $k$  at iteration  $\ell+1$ . Hence, if a face  $j$  is on the boundary of the problem domain  $V$ , then the boundary condition is used to define the incoming angular flux; otherwise the internal or external values angular fluxes are used depending on the orientation of the cell face with respect to the quadrature direction. The boundary conditions we consider are either vacuum,  $\Gamma(\hat{\Omega}_m) = 0$ , or reflection,  $\Gamma(\hat{\Omega}_m) = \psi_{m',i,j}$  for  $m'$  where  $(\hat{\Omega}_{m'} \cdot \hat{n}_j) = |\hat{\Omega}_m \cdot \hat{n}_j|$  and  $(\hat{\Omega}_{m'} \times \hat{\Omega}_m) \cdot \hat{n}_j = 0$ .

For quadrature angle  $\hat{\Omega}_m$ , the transport discretization computes a the angular flux,  $\psi_{m,i,j}$  for each vertex  $j$  on every cell  $k$ . We can write Eq. 23 in matrix notation as

$$\mathbf{T}_m \psi_m^{\ell+1} = \mathbf{S} \phi^\ell + \mathbf{Q}_m, \quad \phi^\ell = \sum_m w_m \psi_m^\ell, \quad (25)$$

where  $\psi_m$  is the vector of discontinuous angular fluxes unknowns in the mesh for angle  $\hat{\Omega}_m$ ,  $\phi$  is the vector of scalar fluxes constructed from  $\psi_m$  for all  $m$  at the previous iteration  $\ell$ , and  $\mathbf{Q}_m$  is the source vector contributing to angle  $\hat{\Omega}_m$  over the mesh. These vectors are in  $\mathbb{R}^{4N_c}$ ,  $N_c$  being the number of cells in the mesh.



With DSA, the source iteration is modified as follows.

$$\psi_m^{\ell+1/2} = \mathbf{T}_m^{-1} \mathbf{S} \phi^\ell + \mathbf{T}_m^{-1} Q_m \quad (26a)$$

$$\phi^{\ell+1/2} = \sum_m w_m \psi_m^{\ell+1/2} \quad (26b)$$

$$\epsilon^{\ell+1/2} = \mathbf{X}^T \mathbf{A}^{-1} \mathbf{X} \Sigma_s (\phi^{\ell+1/2} - \phi^\ell) \quad (26c)$$

$$\phi^{\ell+1} = \phi^{\ell+1/2} + \epsilon^{\ell+1/2} \quad (26d)$$

where  $\mathbf{A}$  represents the  $P_1$  equations, Eqs. 5, with the upwinding equations, Eqs. 7 or 18. Note that the scalar flux transport residuals only contribute a source to the balance equations of the  $P_1$  equations, the moment equations sources being zero. Similarly, the transport scalar fluxes are corrected only by the  $P_1$  equation solution for the scalar fluxes. The matrix  $\mathbf{X}$  is in  $\mathbb{R}^{16N_c \times 4N_c}$ . Because only the balance equation of the  $P_1$  system will have a non-zero source, it has the  $(2 \times 1)$  block form

$$\mathbf{X} = \begin{bmatrix} 0 \\ \mathbf{X}_0 \end{bmatrix}. \quad (27)$$

The block  $\mathbf{X}_0 = I$ , where  $I \in \mathbb{R}^{4N_c \times 4N_c}$  is the identity. The matrix  $\Sigma_s$  is block diagonal, consisting of  $N_c$  blocks, each of which is a  $(4 \times 4)$  matrix containing the scattering cross section in some cell  $k$  on the diagonal. The description of the matrices give here assumes ordering all discontinuous unknowns by vertex and then by cell and the block ordering of the  $P_1$  system unknowns by currents first followed by scalar fluxes.

Boundary conditions for the  $P_1$  equations are reflective when the transport boundary conditions are reflective and vacuum otherwise. The same is true for the boundary conditions used to solve the linear continuous finite element discretized diffusion equation in the two-level preconditioner.

## 2.4 Improving the Efficiency of the Iterative Solution

Krylov iterative methods are used to compute the solution of the discontinuous  $P_1$  equations. We will now suggest two simple ways in which we can reduce the number of Krylov iterations to improve the overall efficiency of the accelerated source iterations.

One way to improve efficiency might be to accept the Krylov subspace GMRES (or MINRES) solution of the  $P_1$  equations after a fixed number of iterations. This can be done as long as the Krylov method converges monotonically in whatever norm is being used to monitor convergence. For general use, though, we consider this approach to be unacceptable because the minimum number of iterations that can be taken without adversely affecting source iteration convergence is not known ahead of time.

Another way would be to relax the convergence tolerance. We found that we could reduce the total

number of iterations spent solving the  $P_1$  equations in the DSA algorithm without affecting the source iteration convergence by varying the convergence tolerance during the course of the  $S_N$  iterations as follows. Let  $E^\ell$  be the discrete  $L_2$  norm of the relative change in cell-average scalar fluxes between two successive  $S_N$  iterations. Then we set the tolerance  $\tau^\ell$  for the GMRES (or MINRES) solver to be proportional to  $E^\ell$ :

$$\tau^\ell = \begin{cases} \frac{1}{10} \max(\frac{1}{10}, \epsilon) & \text{if } \ell = 1 \\ \frac{1}{10} \max(\min(E^\ell, \frac{1}{10}), \epsilon) & \text{otherwise.} \end{cases} \quad (28)$$

Here  $\epsilon$  is the tolerance of  $S_N$  source iteration convergence. The factors of  $1/10$  appearing here are chosen conservatively. We found that this simple heuristic worked very well.

We can also improve the overall efficiency by altering the convergence tolerance of the PCG iterations in the preconditioner for the  $P_1$  equation. We use an approach for improving the solution efficiency of nested inner-outer Krylov methods presented in Ref. 21. This approach can be roughly described by noting that at any particular iteration a Krylov subspace solver constructs a solution based on the solutions from previous iterations to that point. It is therefore logical that the inner iterations should be computed with a strict convergence tolerance in the early stages of the outer iterative solution and the tolerance can be relaxed as the outer iteration proceeds. This is somewhat contrary to intuition and the reasons behind this observation are as yet not fully understood mathematically.<sup>21</sup>

One way to do this would be to make the inner iteration tolerance proportional to the inverse of the norm of the residual of the outer iteration. The discontinuous  $P_1$  equations are solved with just such an inner-outer Krylov method, the outer method in this case being the GMRES( $m$ ) (or MINRES) iteration and the inner method being the PCG iteration for the continuous diffusion equation preconditioner. This is opposite to the strategy we used for the  $S_N$  iterations. Assume that at some iteration  $n$ , the current outer iteration has a residual norm  $r^n$ . Then we set the inner PCG convergence tolerance to

$$\gamma = \begin{cases} \frac{1}{10} \tau & \text{if } n \bmod m = 0 \\ \frac{1}{10} \min(1, \tau / \min(r^n, 1)) & \text{otherwise} \end{cases} \quad (29)$$

where  $\tau$  is the tolerance for the outer iteration. Again, we consider the factors of  $1/10$  to be a conservative choice. In the problems we tried this approach also worked very well, reducing the number of PCG iterations without affecting convergence of the GMRES (or MINRES) iteration. The anticipated improvements in overall efficiency with this approach are limited, however, because the diagonally preconditioned PCG iterations are already very fast.

### 3. FOURIER ANALYSIS

In this section we present a three-dimensional Fourier analysis on tetrahedra. We can use these results to predict how effective DSA methods in accelerating source iteration convergence on unstructured tetrahedral grids.

The underlying Fourier ansatz is made on a three-dimensional Cartesian grid, the basic element of which is a box of dimension  $\Delta x \times \Delta y \times \Delta z$ . The box is divided into six tetrahedra whose edges must line up when the basic elements are “translated” in order to “tile” the Cartesian grid with tetrahedra. The minimum number of tetrahedra that satisfy this requirement is six. This basic element is illustrated in Fig. 3.

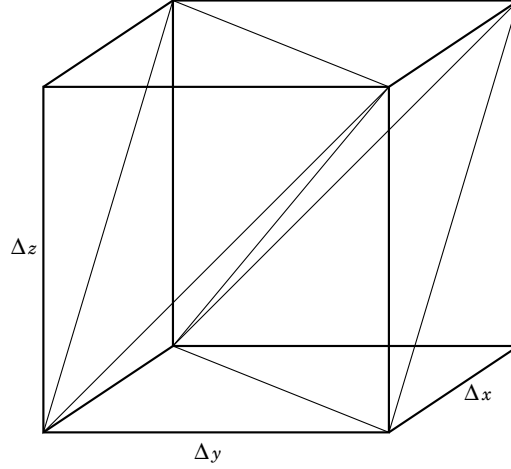


Figure 3. The basic element for the Fourier analysis divided into six tetrahedra of equal volume.

The tetrahedral cells on the basic element are numbered from  $k = 1, \dots, 6$ , each of the four vertices are locally ordered within each tetrahedron from  $j = 1, \dots, 4$ . The four quantities at each vertex in every cell in the basic element are then given the ordering  $i = 4(k - 1) + j$ . The Fourier ansatz assumes the error modes in the quantities  $\Phi_i, J_i^x, J_i^y, J_i^z, i = 1, \dots, 24$ , can be represented in the discrete form

$$\Phi_{j,k}(\mathbf{r}) = \hat{\Phi}_i e^{i(\bar{\Lambda} \cdot \mathbf{r})} \quad (30a)$$

$$J_{j,k}^x(\mathbf{r}) = \hat{J}_i^x e^{i(\bar{\Lambda} \cdot \mathbf{r})} \quad (30b)$$

$$J_{j,k}^y(\mathbf{r}) = \hat{J}_i^y e^{i(\bar{\Lambda} \cdot \mathbf{r})} \quad (30c)$$

$$J_{j,k}^z(\mathbf{r}) = \hat{J}_i^z e^{i(\bar{\Lambda} \cdot \mathbf{r})}. \quad (30d)$$

Here,  $\bar{\Lambda} = [\lambda_x, \lambda_y, \lambda_z]^T$  is the vector of Fourier wave numbers. The terms for cells in the basic element that have faces on the boundary and which exist outside the basic element (the “external” terms  $\Phi_k^{ext}$  and  $\mathbf{J}_k^{ext}$  in Eqs. 7 or 18) are defined in terms of quantities interior to the basic element that are “translated” by the width of the basic element through the Fourier ansatz.

To describe this process in more detail, consult the illustration in Fig. 4. Consider the quantities that

happen to have global indices  $i = 14, 15, 16$  and suppose they are located in a cell on the three vertices of a cell face that is on the left side of the basic element. Remember that although the locations of the quantities are shown to lie just inside the vertices for illustration they are actually defined mathematically as limiting values of the unknowns as the vertices are approached from within the cell. Now suppose that another cell *outside* the basic element (not shown in the figure) has one of its faces on the right side of the basic element and shares this face with the shaded cell inside the basic element, shown in the figure. The boundary terms that couple the shaded cell to those in the adjacent cell sharing this face on the right side of the basic element are denoted by a, b and c in the figure. The Fourier ansatz for the quantities outside the basic element at those points, coming from the “exterior” values in the upwinding equations, “look like” the quantities at  $i = 14, 15, 16$  that are inside the basic element. We choose the “origin” of the basic element to be the vertex at the rear lower left corner of the basic element in Fig. 4. Thus, when the equations for the shaded cell are constructed, the upwind boundary terms are from the adjacent cell at the points a, b and c are assigned the “translated” values of the basic quantities as follows:

$$\begin{aligned} \text{at point a: } & \hat{\Phi}_{14} e^{i\lambda_y \Delta y}, \quad \hat{J}_{14} e^{i\lambda_y \Delta y}; \\ \text{at point b: } & \hat{\Phi}_{15} e^{i\lambda_y \Delta y}, \quad \hat{J}_{15} e^{i\lambda_y \Delta y}; \\ \text{at point c: } & \hat{\Phi}_{16} e^{i\lambda_y \Delta y}, \quad \hat{J}_{16} e^{i\lambda_y \Delta y}. \end{aligned}$$

Similar assignments are made for each of the cells that have faces adjoining the exterior sides of the basic element.

Using the symbolic algebra program MAPLE, Eqs. 5, together with the upwinding equations, Eqs. 7 or 18, are written for all cells and all vertices on the basic element. The Fourier ansatz, including the translated boundary terms from quantities outside of the basic element, is made in the 96 equations on the basic element. The  $(96 \times 96)$  matrix is denoted by  $\hat{\mathbf{A}}$ . It is computed in terms of the basic element thickness  $\Delta x, \Delta y$ , and  $\Delta z$ , the Fourier wave numbers  $\lambda_x, \lambda_y$  and  $\lambda_z$ , and the *constant* material properties: scattering ratio  $c$  and total cross section  $\sigma_t$ .

For every discrete ordinate  $m$ , a Fourier ansatz of the form

$$\psi_{m,j,k}(\mathbf{r}) = \hat{\psi}_{m,i} e^{i(\bar{\mathbf{A}} \cdot \mathbf{r})} \quad (31)$$

is also made for the errors in the angular fluxes  $\psi_{m,j,k}$  of the transport equation Eq. 23. The basic element quantities are  $\hat{\psi}_{m,i}$ ,  $i = 1, \dots, 24$ . The upwinding Eqs. 24 introduce quantities from outside the basic element which are represented by “translated” quantities from inside the basic element. We use the same global ordering and the same “origin” for the basic element to be consistent the Fourier representation of

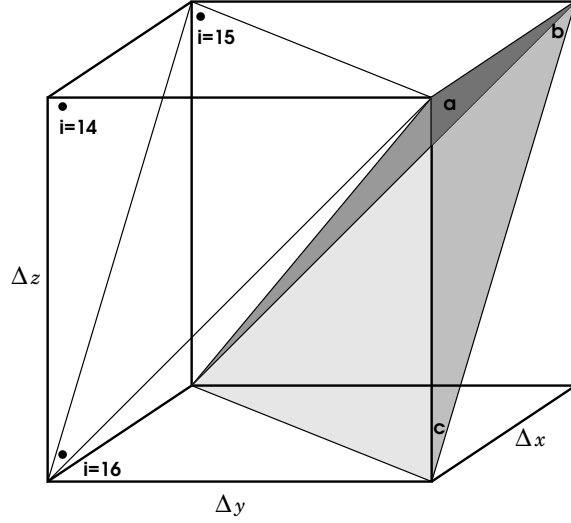


Figure 4. An example illustrating the Fourier ansatz. The cell of interest is shaded. The points a, b and c lie in the cell *outside* the basic element that is adjacent to the shaded cell. The quantities at those points couple the two cells through the discontinuous “upwind” approximation. The upwind terms are represented in the Fourier analysis by the quantities for a cell that lies *inside* the basic element. In this case, quantities at the points a, b and c are assigned “translated” values from the points  $i = 14, 15$ , and 16.

the  $P_1$  equations. In matrix notation, the transport equation can be written for source iteration index  $\ell$  as

$$\hat{T}_m \hat{\psi}_m^{\ell+1} = \sigma_s \sum_m w_m \hat{S} \hat{\psi}_m^{\ell}, \quad (32)$$

where  $\hat{\psi}_m$  represents the vector of Fourier quantities.

For unaccelerated transport, the  $(24 \times 24)$  matrix

$$\hat{F} = \sigma_s \sum_m w_m \hat{T}_m^{-1} \hat{S}, \quad (33)$$

is computed in terms of the Fourier wave number, the basic element thickness, and the material properties using symbolic expressions from MAPLE. The maximum eigenvalue of this matrix is the unaccelerated spectral radius. We have verified that it is equal to  $c = \sigma_s / \sigma_t$ .

Now, the DSA algorithm in Eqs. 26a leads to the  $(24 \times 24)$  matrix ( $\hat{I}$  is the identity)

$$\hat{G} = \left[ \hat{F} + \sigma_s \hat{X}^T \hat{A}^{-1} \hat{X} (\hat{F} - \hat{I}) \right], \quad (34)$$

whose maximum eigenvalue is the spectral radius of the accelerated transport solution. The matrix  $\hat{X}$  is a “projection” matrix of dimensions  $(96 \times 24)$  corresponding to  $\mathbf{X}$  in Eqs. 26a.

The matrix  $\hat{G}$  is computed with MAPLE by combining symbolic expressions for  $\hat{A}^{-1}$ ,  $\hat{F}$ , and  $\hat{X}$ . It is

evaluated for fixed parameters and maximized over all frequencies using a Nelder–Mead simplex algorithm<sup>22</sup> with quadratic surface fitting near suspected maxima. We found this algorithm to be essential in searching for the maximum over the three–dimensional space of wave numbers on  $[0, 2\pi)^3$ .

We end this section by giving an expression for the analytical spectral radius of the DSA algorithm,  $\rho_0$ :<sup>4, 6</sup>

$$\rho_0 = \max_{\lambda_x, \lambda_y, \lambda_z} \left| \omega + \frac{c}{\alpha} (\omega - 1) \right|, \quad (35a)$$

$$\text{where} \quad \omega = \frac{c}{4\pi} \int_{4\Pi} d\Omega \left[ 1 + i (\bar{\Lambda} \cdot \hat{\Omega}) \right]^{-1} \quad (35b)$$

$$\text{and} \quad \alpha = \frac{1}{3} (\bar{\Lambda} \cdot \bar{\Lambda}) + (1 - c). \quad (35c)$$

We evaluate the integral in Eqs. 35 with a discrete ordinates quadrature in which case we denote the discrete ordinates analytical spectral radius corresponding to that quadrature by  $\tilde{\rho}_0$ . Again, we use the simplex algorithm to search over the space of Fourier wave numbers on  $[0, 2\pi)^3$ .

#### 4. NUMERICAL RESULTS

In this section we will investigate the effectiveness and efficiency of the fully consistent DSA (FCDSA) scheme using our solution method for the  $P_1$  equations. Fourier analysis predictions and measurements of the spectral radius will be given for the FCDSA scheme will be compared to those of the partially consistent M4S DSA scheme.<sup>8</sup> In all the computations reported here, we use Algorithm 1 with  $\tilde{\mathbf{A}} = \mathbf{B}$  to solve Eq. 20 using GMRES(15). Note that same algorithm can accelerate the M4S DSA equations. Numerical results are computed using our implementation code, ATTILAV2, as described in Ref. 1. Theoretical predictions of the spectral radius are computed using the results of the Fourier analysis of Section 3. We consider only isotropic scattering in which case we expect the fully consistent method to be stable and effective for all cell widths and cell aspect ratios.

The first set of results, shown in Fig. 5, compares the spectral radius predicted by Fourier analysis to the measured spectral radius from the ATTILAV2 transport code for a scattering ratio  $c = 0.9999$  and total cross section  $\sigma_t = 3.5\text{cm}^{-1}$  with an  $S_4$  triangular, Chebyshev-Legendre (TCL) quadrature. The results are shown as a function of decreasing aspect ratio. The aspect ratio is defined as the three times the ratio of the inscribed sphere radius to the radius of the circumscribed sphere. It is less than or equal to one, attaining its maximum for a tetrahedron with edges of equal length and approaching zero as the tetrahedra become more distorted.<sup>23</sup>

The spectral radius measurements are computed on a fixed  $(8 \times 8 \times 8)$  grid of boxes, each divided into six tetrahedra, for a total of 3072 cells in the problem. The minimum aspect ratios,  $\alpha_{min}$ , are listed in Table I in terms of the dimensions of the basic elements used to generate the results shown in Fig. 5.

The outer problem dimensions are fixed to achieve the desired aspect ratios; for example, to have a basic element of size (2.0 cm  $\times$  1.0 cm  $\times$  5.0 cm), the problem domain is  $x \in [0, 16 \text{ cm}]$ ,  $y \in [0, 8 \text{ cm}]$ ,  $z \in [0, 40 \text{ cm}]$ . Boundary conditions on the bottom, left, and back faces of the problem are reflective, the others are vacuum.

Table I. Minimum aspect ratios,  $\alpha_{min}$ , in terms of the dimensions  $\Delta x$ ,  $\Delta y$ , and  $\Delta z$ , of the basic element.

$\Delta x$ (cm)	$\Delta y$ (cm)	$\Delta z$ (cm)	$\alpha_{min}$
1.0	1.0	1.0	0.632
2.0	2.0	3.0	0.562
1.0	1.0	2.0	0.487
2.0	2.0	5.0	0.421
2.0	1.0	3.0	0.370
3.0	1.0	3.0	0.327
2.0	1.0	5.0	0.256
2.0	1.0	8.0	0.170
8.0	1.0	10.0	0.116

Sources are set to zero and the angular fluxes are initialized randomly. At the end of every  $S_N$  iteration the discontinuous scalar fluxes in the problem are normalized by the sum of the scalar fluxes over the entire mesh. This bounds the scattering source and enables us to compute an asymptotic value of the spectral radius in the event that a DSA scheme is unstable. We use a convergence criterion of  $10^{-4}$  for the inner iterative solution of the  $P_1$  equations and a convergence criterion of  $10^{-5}$  for the PCG iterations used in the two-level preconditioner for the  $P_1$  equations. Convergence is measured by the  $L_2$  norm of the residual relative to the  $L_2$  norm of the source vector in both cases. The spectral radius is measured as the ratio of the change in the  $L_2$  norm of the scalar fluxes over the mesh between successive  $S_N$  iterations. Results are reported at the end of 100 iterations for the FCDSA and M4S methods. The WLA method results are reported after 300 iterations. These results indicate that the fully consistent DSA method is stable and effective whereas the partially consistent method of Adams and Martin can be unstable when the aspect ratio is small. The measured spectral radius is expected to be less than the Fourier analysis predicts because of leakage from the vacuum boundaries. The M4S and WLA methods show a strong dependence on cell aspect ratio and cell thickness. The M4S method becomes unstable as the aspect ratio decreases. This is an unexpected result since the initial verification of the method in one-dimensional slab geometry and two-dimensional rectangular mesh cells did not indicate any instability.<sup>8</sup> The spectral radius of the WLA method increases as the aspect ratio decreases. However, we want to emphasize that this is for a scattering ratio very close to unity and in general the method is very effective when the scattering ratio is not so

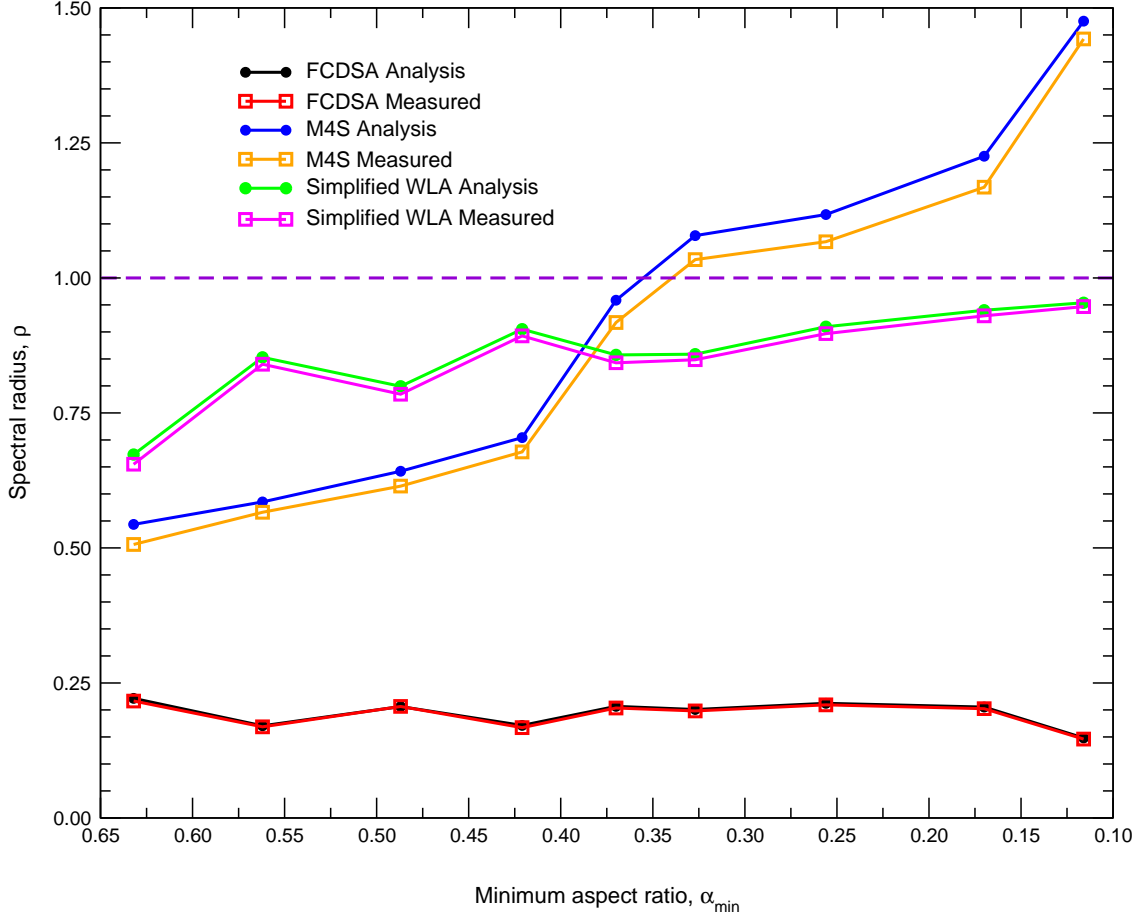


Figure 5. Fourier analysis and computationally measured spectral radius for DSA-accelerated transport for the  $S_4$  TCL quadrature. The spectral radius is shown as a function of decreasing aspect ratio.

close to one. Nonetheless, in applications any degradation in effectiveness of the WLA DSA scheme is often compensated by its computational efficiency. The fully consistent method is largely insensitive to cell aspect ratio.

The next set of results are shown in Fig. 6. We compare the measured spectral radius and the Fourier analysis for the three DSA schemes as before and the scattering ratio is again taken to be  $c = 0.9999$ . This time, though, the total cross section is varied logarithmically from  $2^{-5}\text{cm}^{-1}$  to  $2^{10}\text{cm}^{-1}$  and the basic element size is fixed at  $(2.0\text{ cm} \times 1.0\text{ cm} \times 8.0\text{ cm})$  for which the minimum cell aspect ratio is 0.170. The measured spectral radius is computed on a  $(6 \times 6 \times 6)$  grid of boxes, each divided into six tetrahedra, for a total of 1296 cells and the problem domain is fixed at  $x \in [0, 12\text{ cm}]$ ,  $y \in [0, 6\text{ cm}]$ ,  $z \in [0, 48\text{ cm}]$ . The boundary conditions again consist of three reflective faces and three vacuum faces. The spectral radius  $\rho$  is expected to approach the discrete ordinates analytical value  $\tilde{\rho}_0$  in the limit of vanishing cell thickness and should approach zero for optically thick cells.<sup>4,6</sup> The discrete ordinates analytical spectral radius for the  $S_4$



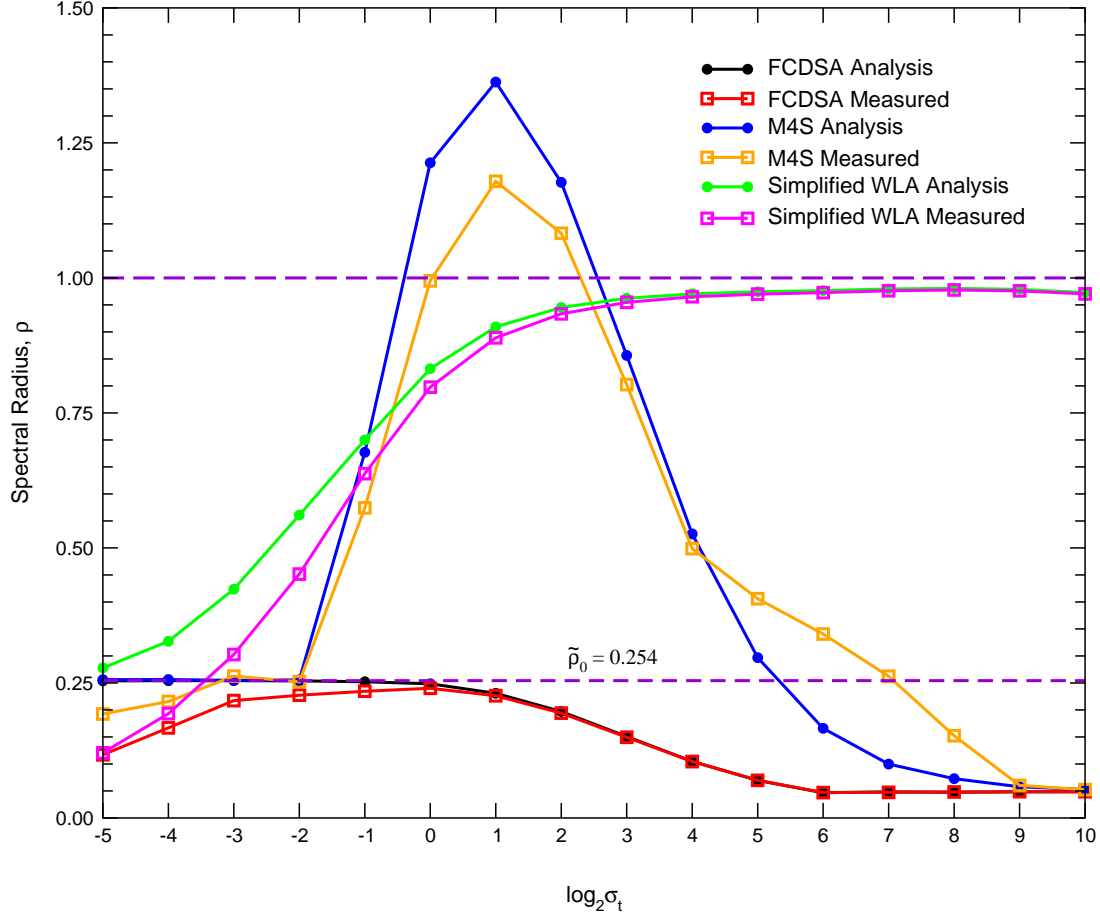


Figure 6. Fourier analysis and computationally measured spectral radius for DSA-accelerated transport for the  $S_4$  TCL quadrature. The spectral radius is shown as a function of total cross section.

TCL quadrature,  $\tilde{\rho}_0 = 0.254$ , is shown in the figure for comparison. For thin cells, the Fourier analysis indeed approaches the analytical value. The measured results drop off from the exact result because of leakage as the problem becomes extremely thin. The fully consistent scheme is stable and effective for all cell optical thickness. The M4S method becomes unstable for intermediate optical thickness. While both the FCDSA and M4S methods become increasingly effective as the problem becomes thick and diffusive, the effectiveness of the WLA method degrades with increasing optical thickness.

The last set of results compares the computational effort needed to compute an  $S_N$  solution with the FCDSA method to that of the WLA DSA scheme. For this problem, we solve a one-group, steady state, oil well logging tool problem, a 139.7 cm tall half cylinder of radius 60 cm, modeled with an unstructured mesh of 43,012 cells.<sup>11</sup> There are two He-3 detectors and a unit source of neutrons inside the problem. The minimum aspect ratio for the mesh is 0.1234 while the maximum is 0.9996. The material cross-sections are given in Table II. Isotropic scattering is assumed for all materials.

Table II. Neutron cross sections for the oil well logging tool problem.

Material	Cross sections ( $\text{cm}^{-1}$ )	
	Total	Scattering
Limestone	$8.79672 \cdot 10^{-1}$	$8.70516 \cdot 10^{-1}$
Iron	$1.16776 \cdot 10^0$	$9.66125 \cdot 10^{-1}$
Water	$3.13459 \cdot 10^0$	$3.11519 \cdot 10^0$
He-3	$4.94621 \cdot 10^{-1}$	$1.00243 \cdot 10^{-4}$

The number of floating point operations (FLOP) needed to compute the  $S_N$  solution to a relative maximum pointwise convergence criteria of  $10^{-5}$  in the scalar fluxes on an SGI Origin 2000 processor are shown in Fig. 7 for a range of TCL quadrature orders  $N$ . The FLOP count is a measure of computational effort not affected by memory access issues and is independent of data layout or other system resource use.

The highly scattering, diffusive water-containing regions of the problem brings the unaccelerated spectral radius to approximately 0.9916. This is the measured spectral radius for the  $S_4$  quadrature which needed  $266.4 \cdot 10^9$  FLOP to converge in 2234 iterations. The FLOP count is proportional to the solution time; for comparison, the unaccelerated solution took 215 CPU minutes to complete. Noting that this is only a one group problem (the cross sections correspond to the lowest neutron energy group in a 47 group library), it is clear that DSA is necessary for practical applications.

The low aspect ratio cells present in this mesh causes the M4S DSA method to be unstable for this problem. We found that after the third iteration with the  $S_4$  quadrature the spectral radius is 1.5136 and the method never recovers. This observation is independent of quadrature order.

The inset of Fig. 7 shows that the simplified WLA method is very efficient, taking a very small fraction of the total solution time. In contrast, the FCDSA algorithm takes a majority of the computation time. However, because it is so effective in reducing the spectral radius – FCDSA converged in 13 iterations and WLA in 102 for all quadratures – the overall computation time can be less than that of the WLA method when the quadrature order is large enough.

## 5. CONCLUSIONS

We have found that our fully consistent DSA scheme for DFEM discretizations of the  $S_N$  equations based on an analogous DFEM discretization of the  $P_1$  equations is stable and very effective over a wide range of cell shapes, dimensions and optical thicknesses. For problems with a low aspect ratio, we found that the partially consistent M4S DSA scheme can be unstable on unstructured grids while the effectiveness of the WLA DSA method degrades for optically thick, diffusive problems. Our results were verified both analytically using our three-dimensional Fourier analysis and numerically with the implementation code ATTILAV2. Degradation

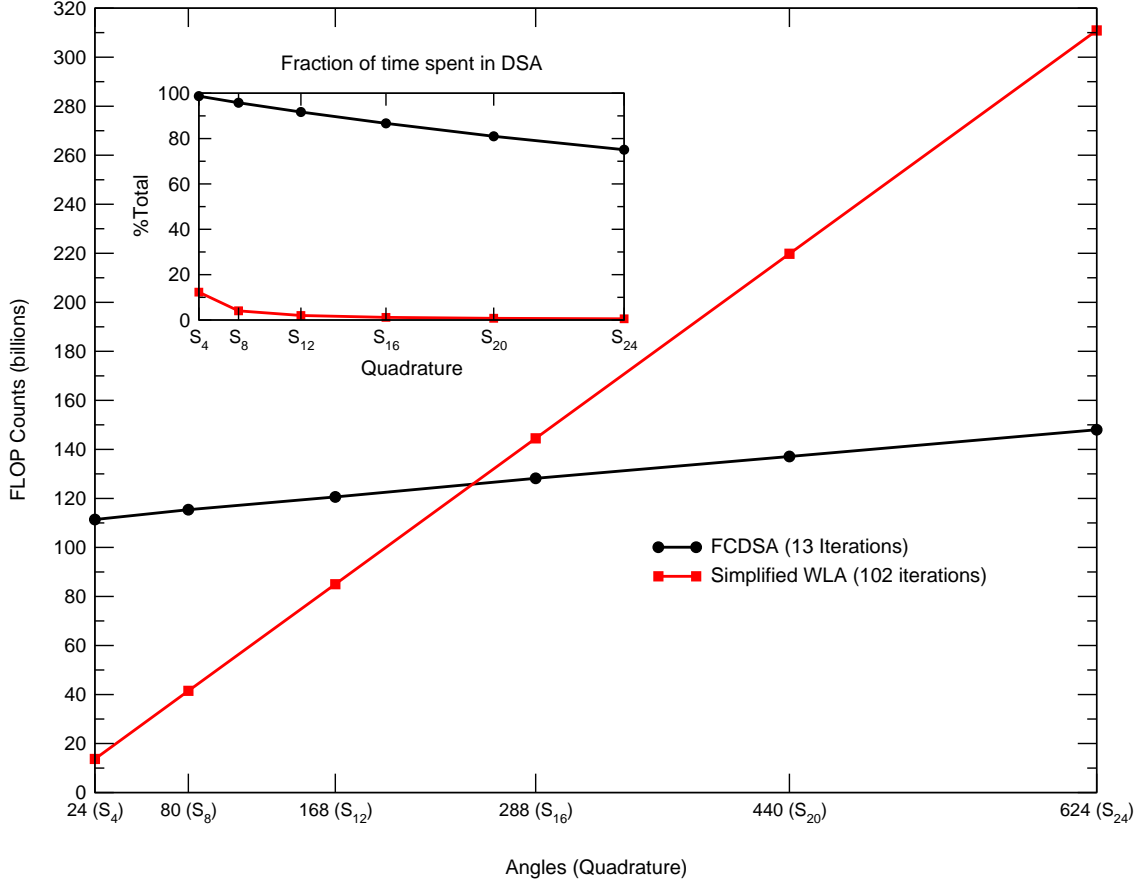


Figure 7. Floating point operation counts (in billions) for the oil well logging tool problem for increasing  $S_N$  quadrature order. The inset shows the percentage of the total FLOP counts used in the DSA algorithm.

of the WLA method in very diffusive and thick problems was expected. On the other hand, the instability of the M4S method was not anticipated in view of the previous work in one and two dimensions. The M4S DSA scheme should probably not be implemented for general use because it is not known in advance if the method will be stable for any given problem.

We expected that the increased complexity of the fully consistent DSA scheme could make it impractical for some problems. But it could be more computationally efficient than the partially consistent WLA DSA method under certain circumstances. For example, a problem may require a high quadrature order because it contains both streaming regions and diffusive regions. We have seen that the fully consistent method was indeed more efficient in that situation. The most promising application for the fully consistent method is probably thermal radiative transfer in the stellar regime, where the scattering ratio is often extremely close to one.

So far we have implemented our methods in serial codes only. Our conclusions could change when

we extend our method to parallel platforms. For instance, solving the symmetric form of the discontinuous  $P_1$  equations with MINRES, even with the less efficient symmetrized preconditioner, could outperform GMRES( $m$ ) in parallel. Or, possibly, the computational efficiency of direct methods might be competitive with iterative methods in parallel implementations. For example, concern over the increased memory requirements associated with fill-in of the matrix during factorization is alleviated to some extent on a distributed memory platform. A discussion of the issues involved in choosing a solution method for linear systems on parallel machines can be found in Ref. 24.

Finally, we plan to pursue methods for solving the reduced Schur complement system for use in DSA applications. Solving the reduced system could make the fully consistent DSA method more competitive. There are applications other than DSA that require the full discontinuous  $P_1$  solution. In that case an efficient solution of the reduced system could be used as part of a very effective preconditioner for the full system. Furthermore, we may be able to compute approximate Schur complement systems that could serve as stable and effective DSA schemes. We are currently exploring these possibilities.

### Acknowledgments

The authors would like to thank Michele Benzi for his advice and perspective on the linear algebraic aspects of and the Krylov solution methods used in this work. This work was performed under the auspices of the U.S. Department of Energy at the Los Alamos National Laboratory.

## References

1. T. A. Wareing, J. M. McGhee, J. E. Morel, and S. D. Pautz, “Discontinuous Finite Element  $S_n$  Methods on Three-Dimensional Unstructured Grids,” *Nuclear Science and Engineering*, **138**, pp. 1–13 (2001).
2. E. M. Gelbard and L. A. Hageman, “The Synthetic Method as Applied to the  $S_n$  Equations,” *Nucl. Sci. and Engr.*, **37**, pp. 288–298 (1969).
3. R. E. Alcouffe, “Diffusion Synthetic Acceleration Methods for Diamond-Differenced Discrete-Ordinates Equations,” *Nucl. Sci. and Engr.*, **64**, pp. 344–355 (1977).
4. E. W. Larsen, “Unconditionally Stable Diffusion-Synthetic Acceleration Methods for Slab Geometry Discrete Ordinates Equations. Part I: Theory,” *Nucl. Sci. and Engr.*, **82**, pp. 47–63 (1982).
5. D. R. McCoy and E. W. Larsen, “Unconditionally Stable Diffusion-Synthetic Acceleration Methods for Slab Geometry Discrete Ordinates Equations. Part II: Numerical Results,” *Nucl. Sci. and Engr.*, **82**, pp. 64–70 (1982).
6. M. L. Adams and T. A. Wareing, “Diffusion-Synthetic Acceleration Given Anisotropic Scattering, General Quadratures, and Multidimensions,” *Trans. of the Am. Nucl. Soc.*, **68**, pp. 203–204 (1993).
7. T. A. Wareing, E. W. Larsen, and M. L. Adams, “Diffusion Accelerated Discontinuous Finite Element Schemes for the  $S_n$  Equations in Slab and X-Y Geometries,” in **Proc. International Topical Meeting on Advances in Mathematics, Computations, Reactor Physics**, Vol. 3, Pittsburgh, Pennsylvania, pp. 11.1 2–1 (28 April – 2 May 1991).
8. M. L. Adams and W. R. Martin, “Diffusion Synthetic Acceleration of Discontinuous Finite Element Transport Iterations,” *Nucl. Sci. and Engr.*, **111**, pp. 145–167 (1992).
9. J. E. Morel, J. E. Dendy, and T. A. Wareing, “Diffusion-Accelerated Solution of the Two-Dimensional  $S_n$  Equations with Bilinear-Discontinuous Differencing,” *Nucl. Sci. and Engr.*, **115**, pp. 304–319 (1993).
10. J. S. Warsa, T. A. Wareing, and J. E. Morel, “Solution of the Discontinuous  $P_1$  Equations in Two-Dimensional Cartesian Geometry with Two-Level Preconditioning,” *SIAM Journal on Scientific Computing* (2000). To appear.
11. T. A. Wareing, J. M. McGhee, and J. E. Morel, “ATTILA: A Three-Dimensional, Unstructured Tetrahedral Mesh Discrete Ordinates Transport Code,” *Transactions of the American Nuclear Society*, **75**, pp. 146–147 (1996).
12. D. N. Arnold, F. Brezzi, B. Cockburn, and D. Marini, “Discontinuous Galerkin Methods for Elliptic Problems,” in **Discontinuous Galerkin Methods** (B. Cockburn, G. E. Karniadakis, and C.-W. Shu, Eds.), 89, Berlin-Heidelberg: Springer-Verlag (2000).

13. B. Cockburn, G. E. Karniadakis, and C.-W. Shu, Eds., **Discontinuous Galerkin Methods**. Berlin–Heidelberg: Springer–Verlag (2000).
14. O. C. Zienkiewicz and R. L. Taylor, **The Finite Element Method**, Vol. 1. London: McGraw–Hill, Fourth Edition (1994).
15. R. J. LeVeque, **Numerical Methods for Conservation Laws**. Basel: Birkhauser Verlag (1990).
16. C. Hirsch, **Numerical Computation of Internal and External Flows**, Vol. 1 *Fundamentals of Numerical Discretization*. New York: Wiley (1988).
17. S. L. Campbell, I. C. F. Ipsen, C. T. Kelley, and C. D. Meyer, “GMRES and the Minimal Polynomial,” *BIT*, **36**, pp. 664–675 (1996).
18. N. M. Nachtigal, S. C. Reddy, and L. N. Trefethen, “How Fast Are Nonsymmetric Matrix Iterations?,” *SIAM Journal on Matrix Analysis and Applications*, **13**, pp. 778–795 (1992).
19. Y. Saad, **Iterative Methods for Sparse Linear Systems**. Boston: PWS Publishing Company (1996).
20. A. Greenbaum, **Iterative Methods for Solving Linear Systems**. Philadelphia: SIAM (1997).
21. A. Bouras and V. Frayssé, “A Relaxation Strategy for Inexact Matrix–Vector Products for Krylov Methods,” CERFACS TR/PA/00/15, European Centre for Research and Advanced Training in Scientific Computation, Toulouse, France (Sept. 2000). *SIAM Journal on Matrix Analysis and Applications*. Submitted.
22. J. A. Nelder and R. Mead, “A Simplex Method for Function Minimization,” *The Computer Journal*, **7**, pp. 308–313 (1965).
23. A. Liu and B. Joe, “Relationship Between Tetrahedron Shape Measures,” **34**, pp. 268–287 (1994).
24. I. S. Duff and H. A. van der Vorst, “Developments and Trends in the Parallel Solution for Linear Systems,” CERFACS TR/PA/99/10, European Centre for Research and Advanced Training in Scientific Computation (Apr. 1999).